What controls the variability of CO_2 fluxes in eastern boundary upwelling systems?

Riley X. Brady[1], Nicole S. Lovenduski[1], Michael A. Alexander[2], Michael Jacox[3], and Nicolas Gruber[4]

[1]Department of Atmospheric and Oceanic Sciences and Institute for Arctic and Alpine Research, University of Colorado, Boulder, CO, USA
[2]NOAA/ESRL, Boulder, CO, USA
[3]University of California, Santa Cruz, CA and NOAA/SWFSC, Monterey, CA, USA
[4]Environmental Physics, Institute of Biogeochemistry and Pollutant Dynamics, ETH Zürich, Zürich, Switzerland

Correspondence to: Riley X. Brady (riley.brady@colorado.edu)

Abstract. Eastern Boundary Upwelling Systems (EBUS) are governed by alongshore, equatorward winds that force cold, corrosive, and nutrient-enriched waters to the surface. The complex physical and biological dynamics of these regions leads to a temporally variable mosaic of air-sea CO_2 fluxes with some of the highest flux densities globally. This variability can dictate when we might expect the anthropogenic signal of CO_2 flux to become emergent in each system. In this study, we diagnose the physical and biological mechanisms that control historical (1920-2015) CO_2 fluxes in the four major EBUS: the California (CalCS), Humboldt (HumCS), Canary (CanCS), and Benguela Currents (BenCS). We utilize biogeochemical output from the CESM Large Ensemble, a global coupled climate model ensemble that is forced under historical and RCP8.5 radiative forcing. Differences between simulations can be attributed entirely to internal climate variability, as simulations are generated by introducing round-off perturbations to the initial atmospheric temperature. This experimental setup provides us with 34 independent and unique representations of internal climate variability, allowing us to robustly assess variability in CO_2 fluxes. We find that anomalous CO_2 flux in the CalCS and CanCS is most associated with oscillations in oceanic and atmospheric subtropical gyres: the North Pacific Gyre Oscillation (NPGO) and the North Atlantic Oscillation (NAO), respectively. The CalCS (CanCS) has anomalous uptake (outgassing) of carbon during the positive phase of the NPGO (NAO). The HumCS responds mainly to El Niño Southern Oscillation (ENSO), with anomalous uptake of CO_2 during an El Niño event. Variations in dissolved inorganic carbon (DIC) and sea surface temperatures (SST) are the major contributors to these anomalous fluxes, and are generally driven by changes to upwelling, the mixed layer depth, and biology. A better understanding of the sensitivity of CO_2 fluxes in EBUS to internal climate variability might lead to some short-term predictive skill in the ocean–atmosphere carbon cycle. Skillful prediction would be particularly useful in forecasting and managing the onset of ocean acidification in systems that have a naturally low pH and carbonate ion concentration.

1 Introduction

The four major Eastern Boundary Upwelling Systems (EBUS) occur at the eastern edges of subtropical gyres in the Atlantic and Pacific oceans – the California Current System (CalCS), Humboldt Current System (HumCS), Canary Current System

(CanCS), and Benguela Current System (BenCS). These regions are characterized by semi-permanent or permanent equatorward winds that drive both coastal Ekman upwelling and curl-driven Ekman pumping within the first 200km of the coastline (Chavez and Messié, 2009). Upwelling delivers deep waters with respired nutrients to the surface, fueling fisheries that are highly productive with respect to the small surface area they cover (Ryther, 1969). This process also supplies waters with an elevated dissolved inorganic carbon (DIC) content, which enhances the partial pressure of carbon dioxide (pCO_2) and reduces the pH and carbonate ion concentration. In turn, these systems are naturally sensitive to the impacts of ocean acidification (Hauri et al., 2009; Bakun et al., 2015; Chan et al., 2017).

The carbonate chemistry of EBUS is controlled by a complex interplay of physical and biological processes: entrainment of subsurface waters, horizontal advection, upwelling and vertical mixing, temperature changes, photosynthesis, respiration, and calcium carbonate formation and dissolution (DeGrandpre et al., 1998; King et al., 2007). These terms combine to dictate oceanic pCO_2, which drives the pCO_2 gradient between the ocean and atmosphere (ΔpCO_2), thus contributing to the magnitude and determining the direction of air-sea CO_2 fluxes.

Although coastal oceans around the world have small contributions to the global carbon flux, they are characterized by a high CO_2 flux density, or the magnitude of air-sea carbon exchange per unit area (Laruelle et al., 2010, 2014; Gruber, 2015). Low-latitude upwelling systems, such as the HumCS and CanCS, tend to be net outgassing systems, due to their relatively warm waters and persistent upwelling. Because of their colder temperatures and active biology, mid-latitude systems, such as the CalCS and BenCS, act as weak CO_2 sinks that can become CO_2 sources during certain seasons (Borges and Frankignoulle, 2002; Hales et al., 2005; Cai et al., 2006; Gregor and Monteiro, 2013). Surface ocean pCO_2 and thus air-sea CO_2 flux in EBUS exhibits high temporal variability at sub-seasonal, seasonal, and interannual time scales (Friederich et al., 2002; González-Dávila et al., 2009; Leinweber et al., 2009; Evans et al., 2011; Turi et al., 2014). Although the pronounced temporal variability of CO_2 fluxes in EBUS has been documented by a number of studies, little work has been done to associate it directly with internal climate variability.

It has long been recognized that EBUS have intense variations in biology that are coupled to large-scale physical variability (*e.g.*, Chelton et al., 1982; Barber and Chavez, 1983; Barber and Chávez, 1986). Studies have associated this variability with major climate indices, such as the El Niño Southern Oscillation (ENSO; Barber and Chavez, 1983; Barber and Chávez, 1986; Lynn and Bograd, 2002; Chavez et al., 2002; Escribano et al., 2004; Frischknecht et al., 2015), Pacific Decadal Oscillation (PDO; Mantua et al., 1997; Chhak and Di Lorenzo, 2007; Chenillat et al., 2012), North Pacific Gyre Oscillation (NPGO; Di Lorenzo et al., 2008, 2009; Chenillat et al., 2012), and North Atlantic Oscillation (NAO; Borges et al., 2003; Cropper et al., 2014). A similar analysis for EBUS CO_2 fluxes is necessary for the community. Identifying robust relationships between modes of climate variability and CO_2 fluxes would (1) advance our understanding of the complex carbonate system in EBUS and (2) provide some level of predictability in CO_2 flux anomalies. EBUS are naturally sensitive to ocean acidification and have internal variability that rivals the magnitude of the seasonal cycle. Thus, forecasting anomalous CO_2 fluxes could aid in detecting the early onset of seasonal ocean acidification (Landschützer et al., 2018; Kwiatkowski and Orr, 2018; Hauck, 2018).

Previous studies have utilized observations (*e.g.*, Boyd et al., 1987; Friederich et al., 2002; Chavez et al., 2002; Santana-Casiano et al., 2007; Di Lorenzo et al., 2008, 2009) and output from high-resolution hindcast simulations (Jacox et al., 2015;

Frischknecht et al., 2015, 2017; Turi et al., 2017; Mogollón and Calil, 2017) to explore the relationship between climate variability and EBUS biogeochemistry. However, single realizations, whether modeled or observed, provide a limited sample size of internal variability. At most, hindcast model runs and observational time series capture 10 El Niño and 10 La Niña events, and only 1 phase of the PDO. This is problematic, because mid-latitude atmospheric noise can obscure the signal of climate modes such as ENSO, causing a diversity of responses in EBUS (Deser et al., 2017, 2018). Thus, one requires many more case studies to robustly assess the response of EBUS biogeochemistry to internal variability. A solution to this problem is to use a single-model ensemble that is derived by introducing perturbations to the initial state of the climate system. This gives rise to a set of realizations with unique representations of internal climate variability and gives one access to many hundred ENSO events, rather than just a handful. By performing historical experiments with increasing atmospheric CO_2 rather than a long control run, we can account for variability in anthropogenic CO_2 in the ocean as well as potential modifications to the frequency and amplitude of internal variability with climate change (e.g., Timmermann et al., 1999; Kuzmina et al., 2005; Sydeman et al., 2013; Cai et al., 2014, 2015).

In this study, we utilize output from the single-model Community Earth System Model "Large Ensemble" (CESM-LENS; Kay et al., 2015; Lovenduski et al., 2016) to identify major modes of climate variability that are associated with anomalous CO_2 fluxes in the major EBUS. We expand on this by investigating the physical and biological drivers that underpin these anomalies. The single-model ensemble is necessary for such an analysis, since the forced signal can be removed to generate residual simulations that solely represent CO_2 flux responses to internal climate variability (Thompson et al., 2015). Since the simulations are forced with historical CO_2 emissions, each member accounts for the combined response of natural and anthropogenic CO_2 to climate variability. Furthermore, the availability of 34 simulations allows us to find statistically robust relationships between anomalous fluxes and internal variability. This experimental setup addresses the data limitation issues of an observational study as well as the single realization problem of a model hindcast or a multi-model ensemble.

2 Methods and Model Evaluation

2.1 Model Configuration and Upwelling Regions

We utilize monthly output from 34 members of the CESM-LENS, which is derived from a fully coupled Atmosphere-Ocean General Circulation Model (AOGCM) with ocean biogeochemistry (Kay et al., 2015; Lovenduski et al., 2016). Round-off level perturbations are made to the atmospheric temperature in 1920, leading to an ensemble of simulations that diverge solely due to the influence of internally generated variability. This provides us with a set of 34 independent representations of climate variability, with which we can robustly assess the controls on air-sea CO_2 flux variability in EBUS. The ensemble is forced with historical radiative forcing from 1920–2005 and RCP8.5 radiative forcing from 2006–2100. The ocean model has nominal 1^o horizontal resolution with vertical resolution of 10 m through the upper 250 m, thus resolving the Ekman layer. Due to the coarse horizontal resolution, neither curl-driven nor coastal upwelling is directly resolved, but both are represented in the model. A more detailed discussion of coastal upwelling in the CESM-LENS for the CalCS in particular can be found in Brady et al. (2017).

Upwelling regions were confined to approximately the 10^o latitude of most active upwelling as defined by Chavez and Messié (2009), although the CanCS domain was shifted north by 9^o to capture the more intense upwelling off the Western Sahara in CESM1 (Table 11). They were then limited to the first 800km in the offshore direction. The black outlines in Figure 11e–h display these regions. The ensemble mean – which represents both the seasonality and anthropogenic trend for CO_2 flux – was removed from each simulation for each upwelling system to create internally generated residuals. All output was analyzed at monthly resolution.

2.2 Statistical Analysis and Model Equations

Air-sea CO_2 fluxes in CESM are computed following the parameterization of Wanninkhof (2014):

$$F = k \cdot K_0 \cdot (pCO_2^o - pCO_2^a), \tag{1}$$

where k represents the gas transfer velocity (dependent on the wind speed squared), K_0 the solubility of CO_2 in seawater, and $p\mathrm{CO}_2^o$ and $p\mathrm{CO}_2^a$ the partial pressures of CO_2 in the surface ocean and atmosphere, respectively.

We use a linear Taylor expansion to quantify the relative contribution of each variable to the overall CO_2 flux anomaly in response to internally generated variability following Lovenduski et al. (2007) and Turi et al. (2014),

$$\Delta F = \frac{\partial F}{\partial U}\Delta U + \frac{\partial F}{\partial pCO_2^{oc}}\Delta pCO_2^{oc}, \tag{2}$$

where $\frac{\partial F}{\partial U}$ and $\frac{\partial F}{\partial pCO_2^{oc}}$ are determined from the model equations and mean values in each EBUS. Δ's represent the linear regression of the given variable's residuals onto a climate index. The contributions from ΔpCO_2^{oc} is further decomposed into DIC, Alk, SST, and salinity terms:

$$\Delta pCO_2^{oc} = \frac{\partial pCO_2^{oc}}{\partial DIC}\Delta DIC + \frac{\partial pCO_2^{oc}}{\partial Alk}\Delta Alk + \frac{\partial pCO_2^{oc}}{\partial T}\Delta T + \frac{\partial pCO_2^{oc}}{\partial S}\Delta S. \tag{3}$$

Because DIC and Alk can be diluted by freshwater fluxes, we introduce salinity-normalized DIC (sDIC) and Alk (sAlk),

$$\Delta F = \frac{\partial F}{\partial U}\Delta U + \frac{S}{S_0}\frac{\partial F}{\partial DIC}\Delta sDIC + \frac{S}{S_0}\frac{\partial F}{\partial Alk}\Delta sAlk + \frac{\partial F}{\partial fw}\Delta fw + \frac{\partial F}{\partial T}\Delta T + \frac{\partial F}{\partial S}\Delta S. \tag{4}$$

Due to the significance of sDIC anomaly contributions to the total CO_2 flux anomaly in EBUS, we approximate the mechanisms controlling sDIC anomalies following Lovenduski et al. (2007),

$$\frac{d(sDIC')}{dt} = J'_{circ} + J'_{bio} + J'_{ex} \tag{5}$$

where J'_{circ}, J'_{bio}, and J'_{ex} represent the sources and sinks of sDIC′ from circulation, biology, and CO2 flux anomalies integrated over the upper 100m, respectively. See Lovenduski et al. (2007, their Equation 4) for additional details on these terms and their Appendix B for the computation of J'_{bio} in particular.

To compensate for autocorrelation that is characteristic of climate indices and is also introduced from smoothing, we replace the *t*-statistic sample size *N* with an effective sample size, N_{eff}:

$$N_{eff} = N\left(\frac{1 - r_1 r_2}{1 + r_1 r_2}\right) \tag{6}$$

where r_1 and r_2 are the lag-1 autocorrelation coefficients of the two time series being correlated (Bretherton et al., 1999; Lovenduski and Gruber, 2005). N_{eff} represents the number of statistically independent measurements.

2.3 Model Evaluation

CESM-LENS air-sea CO_2 fluxes were compared to the observationally-based SOM-FFN (Self-Organizing Map-Feed Forward Network) product from Landschützer et al. (2017) along the four major EBUS outlined by Chavez and Messié (2009). The SOM-FFN was generated by a two step process. First, the global oceans were grouped into 16 biogeochemical provinces based on common relationships between SSTs, sea surface salinity, mixed layer depth, and pCO_2 climatology from Takahashi et al. (2009). Secondly, nonlinear relationships were determined between an expanded set of predictor variables and the Surface Ocean Carbon Atlas version 4 (Bakker et al., 2016) database of surface ocean CO_2 measurements to interpolate pCO_2 to monthly resolution spanning 1982-2015 at 1^ox1^o global resolution. Extensive details on and validation of the procedure can be found in Landschützer et al. (2013) and Landschützer et al. (2016).

Figure 11 compares the historical climatology (1982–2015) between the SOM-FFN (a–d) and the CESM-LENS (e–h). The Pacific systems are particularly well-modeled. The CESM-LENS simulates the meridional gradient of poleward uptake and equatorward outgassing of CO_2 in the CalCS (Figure 11e). For this system and all other EBUS, we do not expect the model to resolve nearshore outgassing, as coastal upwelling here occurs at the sub-grid scale. In the HumCS, the model depicts the strong outgassing that is characteristic of a tropical upwelling system (Figure 11f). The CO_2 flux climatology in the Atlantic systems is more biased in the CESM-LENS. While the SOM-FFN portrays a meridional gradient of relatively weak CO_2 fluxes in the CanCS, the CESM-LENS simulates strong outgassing along the Western Sahara (Figure 11c and g). An important caveat is that the data density of pCO_2 in EBUS informing the SOM-FFN is on the order of the Southern Ocean, a notably undersampled region (Bakker et al., 2016; Laruelle et al., 2017). In turn, the EBUS CO_2 fluxes are being informed by remote biogeochemical provinces more often than other regions of the ocean. The BenCS has the most biased CO_2 flux climatology of the major EBUS in CESM-LENS. Although it simulates the meridional gradient portrayed in the SOM-FFN, the ougassing cell is nearly 10^o too far south and is significantly stronger than in the SOM-FFN (Figure 11d and h).

The BenCS has the largest physical biases in CESM-LENS than all other EBUS. Its SST bias is in excess of 7^oC with the nominal 1^o atmospheric resolution. Further, it only improves to a 5^oC bias at 0.5^o atmospheric resolution (Gent et al., 2010). This bias is likely driven by the fact that the Angola-Benguela Front is simulated too far south, in addition to deficiencies in upwelling and meridional transport that are driven by unrealistic alongshore wind stress structure (Small et al., 2015). Because of these deficiencies that are specific to the BenCS, we will only discuss its internal variability in CO_2 fluxes in Section 3.1, but will not perform a full analysis on its connections to larger-scale climate variability.

3 Results

3.1 Internal Variability in Upwelling Systems

We emphasize the magnitude of internal variability in EBUS CO_2 fluxes in Figure 12 by showing the ensemble mean standard deviation of air-sea CO_2 flux residuals (ensemble mean subtracted) at each location across the global ocean. Save for the Southern Ocean and subpolar Arctic, the EBUS emerge as significant regions influenced by internal variability on a global scale. The HumCS, CanCS, and BenCS in particular have some of the highest internally driven CO_2 fluxes globally. The CalCS has comparatively low internal variability in CO_2 fluxes. Coastally, the EBUS are distinct from the major western boundary currents, which appear to be influenced very little by internal variability (Figure 12).

Figure 13 (a–d) displays time series of historical CO_2 flux from 1920–2015 and the mean seasonal cycle and monthly magnitude of internal variability (e–h) for each of the four EBUS. The black line depicts the seasonal cycle, the red line the anthropogenically forced trend, and the gray shading the component due to internal variability. Values for each of these components and the linear intercept are reported in Table 11. The largest absolute internal variability is found in the BenCS and HumCS with values of 0.98 mol m^{-2} yr^{-1} and 1.20 mol m^{-2} yr^{-1}, respectively (Table 11). The BenCS is uniquely exposed to variability from the Southern Ocean and Agulhas Current (Reason et al., 2006). The HumCS likely has intense variability due to its direct connection to the tropical Pacific Ocean and thus rapid communication with ENSO (e.g., Colas et al., 2008; Montes et al., 2011).

All four systems have statistically significant trends toward a greater CO_2 sink due to the invasion of anthropogenic carbon (Figure 13; Table 11). This forces the HumCS, CanCS, and BenCS to act as intermittent sinks by 2015 in some realizations due to the combination of the long-term trend and internal variability. The HumCS and BenCS have the largest uptake of anthropogenic CO_2 over the historical period, which is on the order of the magnitude of their seasonal cycles over the course of 96 years. The CanCS is a unique case, where the anthropogenic trend is more than double the magnitude of its seasonal cycle (Table 11). The seasonal cycle of all EBUS excluding the CanCS is approximately sinusoidal with an outgassing peak in the late boreal summer (Figure 13e–h). The CanCS has a relatively weak bi-modal outgassing peak in late winter and early summer, but is otherwise relatively flat (Figure 13g). It has by far the smallest seasonal cycle of the four systems (Table 11).

The magnitude of internal variability is greater than that of the seasonal cycle for the majority of systems. The non-seasonal component of the total variability (the sum of the seasonal and internal components) is 59% for the HumCS, 73% for the CanCS, and 56% for the BenCS (Table 11). Only the CalCS has a stronger seasonal cycle of CO_2 flux than internal variability, but the non-seasonal component still accounts for 33% of the variability in this system (Table 11). Perhaps for the CalCS, more significant internal variability would be captured at a higher resolution that resolves coastal upwelling, such as in Turi et al. (2014, Figure 8c). Lastly, internal variability in CO_2 fluxes tends to be phase-locked with the seasonal cycle for the HumCS and BenCS, as the peak magnitudes of internal variability track the ridges and troughs of the seasonal component (Figure 13f and h). The CanCS has more complex behavior in the residuals due to the bi-modal peaks of its seasonal cycle (Figure 13g), and the CalCS has a relatively uniform magnitude of internal variability throughout the year (Figure 13e).

3.2 California Current

Our primary goal for each EBUS was to identify the dominating mode of climate variability associated with its CO_2 flux residuals. We correlated area-weighted residuals from the black boxes in Figure 11e–h for each simulation with every grid cell globally for a set of predictor variables' residuals: SST, sea level pressure (SLP), 10m wind speed, and wind stress curl. We then assessed the ensemble mean of the correlations to determine the mode of climate variability associated with the given global spatial pattern. Figure 14 displays one ensemble mean correlation case for the CalCS (a), HumCS (b), and CanCS (c) as well as violin plots showing the spread of correlations across the 34-member ensemble for Pacific (Figure 14d–e) and Atlantic (Figure 14f) modes of variability.

The global correlation between CalCS CO_2 flux residuals and SSTa yields a map suggestive of Pacific Decadal Variability, due to the zonal dipole of correlations in the North Pacific (Figure 14a; Mantua and Hare, 2002; Di Lorenzo et al., 2008). Although similar in structure to the PDO, this map most closely resembles the NPGO (Di Lorenzo et al., 2008). In fact, correlations between the NPGO with annual smoothing and CalCS CO_2 flux yields an r-value of -0.49 $\pm$ 0.04. In comparison, linear correlations with the PDO result in an r-value of 0.24 $\pm$ 0.05 (Figure 14d). Thus, we highlight the NPGO as the major mode of climate variability associated with anomalous CO_2 flux in the CalCS. We computed the NPGO index in CESM-LENS following Di Lorenzo and Mantua (2016).

Figure 15a depicts the results of a linear Taylor expansion for CalCS CO_2 flux residuals regressed onto the 1σ positive phase of the NPGO (Eq. 4). Since the area-weighted analysis might be sensitive to the box chosen to represent the CalCS, we also include correlations between individual grid cells and the NPGO in Figure 15b. We find that the CalCS responds uniformly to the NPGO with anomalous uptake of CO_2, intensifying the mean state of the system as an uptake site (Figure 15). The direct regression of ΔF onto the NPGO results in an anomalous uptake of 0.10 mol m^{-2} yr^{-1} (Table 12), which is roughly 24% of the long-term historical mean of -0.42 mol m^{-2} yr^{-1}. The primary contributions to this uptake anomaly come from SST and sDIC, which act in opposition to one another. This is coherent with our definition of the NPGO as the oceanic expression of the atmospheric North Pacific Oscillation (NPO; Di Lorenzo et al., 2008). A positive NPO (and thus NPGO) increases upwelling-favorable conditions in the CalCS through intensification of the North Pacific High (Di Lorenzo et al., 2008). This leads to enhanced upwelling of cold subsurface waters, which increases the CO_2 solubility of the system, contributing toward the uptake anomaly.

Nearly in balance with this term is the influence of sDIC. The enhanced upwelling also delivers remineralized carbon from depth, which increases surface sDIC, contributing to an opposing outgassing anomaly. In fact it is the minor uptake contributions from the remaining terms – wind, salinity, sAlk, and freshwater flux – that pushes the system in favor of anomalous uptake. The CalCS has the largest relative ensemble spread in sDIC and sAlk (Figure 15; Table 12). This is potentially because of inter-simulation variability in the response of CalCS dynamics to the NPGO due to atmopsheric noise (as in the case of ENSO in Deser et al., 2017, 2018) which can directly alter the biogeochemical properties of source waters that feed upwelling (Pozo Buil and Di Lorenzo, 2017). Although the linear Taylor expansions approximates a CO_2 flux anomaly nearly half that of

the direct regression of ΔF onto the NPGO, it is still of the same sign. This discrepancy is due to the influence of higher-order and cross-derivative terms that we did not account for in our approximation.

We also performed this analysis for the CalCS response to a 1σ positive (warm) phase of the PDO (Figure 16a and b). Every simulation displayed a dipole response to the PDO (not shown), with anomalous uptake in the nearshore region south of Cape Mendocino, and anomalous outgassing elsewhere in the domain (Figure 16c). This was the only case in which we found a non-uniform response across all simulations to any mode of climate variability investigated. Both the nearshore and offshore regions have modest correlations with the PDO, with r-values of -0.16 $\pm$ 0.03 and 0.28 $\pm$ 0.05, respectively. The positive phase of the PDO results in anomalously warm SSTs along the CalCS and causes shallower upwelling cells with higher retention of nutrient- and carbon-depleted surface waters (Chhak and Di Lorenzo, 2007). This aligns with the inverted contributions of SST and sDIC in Figure 16a and b relative to the contributions of these terms in response to the NPGO (Figure 15a).

The warming of CalCS SSTs during a positive phase of PDO causes a reduction of CO_2 solubility and thus a tendency toward outgassing (Figure 16). The shallow upwelling cells with less remineralized carbon contribute toward anomalous uptake of CO_2 throughout the system. Note that the nearshore decomposition in Figure 16a has a y-axis range four times smaller than that of the offshore decomposition. This slight uptake anomaly is the result of a delicate balance of minor terms, where the sDIC reduction slightly outweighs the warming effect. On the other hand, the offshore region has contributions from SST and sDIC that are as much as triple the magnitude as that for the NPGO (Table 12). Despite the sDIC reduction being larger than the SST term, the reduced sAlk is substantial enough to cause a slight outgassing anomaly offshore (Figure 16b).

The direct response of winds to the NPGO and PDO plays a negligible role in influencing anomalous CO_2 flux in the CalCS (Table 12). Although ΔU in response to the NPGO and PDO is on the order of the HumCS and CanCS, $\frac{\partial F}{\partial U}$ is 3–10 times smaller than the other systems. $\frac{\partial F}{\partial U}$ is based on the climatological mean U, ΔpCO_2, and Schmidt number. The CalCS has the smallest mean ΔpCO_2 of the EBUS – just 0.2μatm. This causes CO_2 flux in the system to be relatively insensitive to fluctuations in the wind.

3.3 Humboldt Current

Figure 14b shows the ensemble mean global correlation between the HumCS and SSTa. This displays ENSO as the major influence on CO_2 flux anomalies in the HumCS, with regions of high correlation focused around the equatorial Pacific. Correlations between HumCS CO_2 flux anomalies and the Nino3 index resulted in an r-value of -0.40 $\pm$ 0.04 (Figure 14e). Similar results were found for the Nino3.4 index (-0.38 $\pm$ 0.04) and the Nino4 index (-0.36 $\pm$ 0.05). We chose the Nino3 index as our primary predictor of HumCS CO_2 flux anomalies, since it is more eastern-focused and thus captures the stronger spatial correlations closest to the HumCS (Figure 14b).

We present the results of a linear Taylor expansion for HumCS CO_2 flux residuals regressed onto a 1^o El Niño in Figure 17 (Eq. 4). We find that the HumCS responds with a near-uniform CO_2 uptake anomaly, resulting in a weakening of the climatological outgassing site (Figure 17b). Although there is a small region in the northern HumCS that responds with an outgassing anomaly, it is nowhere near as coherent across the ensemble as was the spatial dipole response of the CalCS to the PDO (Figure 16c). The direct regression of ΔF onto the Nino3 index results in an anomalous uptake of 0.49 mol m^{-2} yr^{-1},

which is approximately 18% of the long-term historical mean of 2.8 mol m^{-2} yr^{-1}. As in the case of the CalCS, the two major terms contributing to the uptake anomaly are sDIC and SST, which are in opposition to one another. We would anticipate this to be the case, as an El Niño event induces warming along the HumCS as well as reduces the efficacy of upwelling due to the presence of an anomalously deep thermocline (Strub et al., 1998).

In CESM-LENS, the HumCS experiences a warming of 0.7^oC for a 1^o El Niño, which results in an outgassing pressure of 0.3 mol m^{-2} yr^{-1} (Table 12). However, sDIC in the system is reduced by 13.2 mmol m^{-3} for the same event, which translates to a large uptake contribution of 0.8 mol m^{-2} yr^{-1} (Table 12). This is an enormous change in sDIC, which is partially driven by the high subsurface DIC bias in the east equatorial Pacific in CESM (see Lovenduski et al., 2015, their Figure 2). The large sDIC reduction is due to weakened upwelling and a deepening of the thermocline by advected midequatorial waters.

Lastly, there is a minor outgassing anomaly of 0.06 mol m^{-2} yr^{-1} in response to a slight intensification of winds during El Niño (Table 12). While upwelling-favorable winds tend to decrease along Chile during an El Niño, they generally persist or strengthen along Peru (Wyrtki, 1975; Enfield, 1981; Huyer et al., 1987). Despite the significant contributions of wind speed, SST, and sAlk toward outgassing, the large reduction in sDIC drives an uptake anomaly that weakens the HumCS outgassing during an El Niño event.

3.4 Canary Current

The global correlation between CanCS CO_2 flux anomalies and SLPa are displayed in Figure 14c. Here a region of high positive correlation emerges just northwest of Africa. This encircles the climatological position of the Azores High, the atmospheric subtropical gyre which forces the CanCS. The climate index that most directly captures variability in the Azores High is the NAO, and will thus be considered the main mode of climate variability that modulates anomalous CO_2 flux in the CanCS. We find modest correlations of 0.28 ± 0.03 between annually smoothed CanCS CO_2 flux anomalies and the NAO (Figure 14f). Relatively lower correlations are expected between anomalous EBUS CO_2 fluxes and atmospheric indices, as the atmosphere is noisier than the more slowly evolving ocean.

Grid cell correlations between CanCS CO_2 flux anomalies and the NAO are displayed in Figure 18b. The CanCS has a nearly uniform response of increased outgassing during the positive phase of the NAO. The direct regression of ΔF onto a 1σ NAO results in an outgassing anomaly of 0.2 mol m^{-2} yr^{-1} (Table 12), which is 21% of the historical mean of 0.95 mol m^{-2} yr^{-1}. Also note that the linear Taylor approximation aligns exactly with the direct regression. As with the other EBUS, the major contributors toward this anomaly are sDIC and SST (Figure 18a). Their directions align with that of the CalCS response to the NPGO (Figure 15a). This is expected, as the NAO is the Atlantic analogue to the North Pacific Oscillation (NPO), which forces the NPGO. The NAO describes modifications to the intensity of atmospheric gyre circulation between the Azores High and Icelandic Low.

During the positive phase of the NAO, a stronger Azores High leads to intensified alongshore winds and thus more vigorous upwelling. This brings up additional deep cold water which in turn increases the CO_2 solubility of the system, tending toward an uptake anomaly of 0.15 mol m^{-2} yr^{-1} (Table 12). On the other hand, the increased sDIC from intensified upwelling is double the magnitude of the SST contribution, leading to an outgassing anomaly of 0.33 mol m^{-2} yr^{-1}. This large sDIC response is

driven both by a high $\Delta sDIC$ of 3.9 mmol m^{-3} per 1σ NAO as well as the fact that the CanCS has the highest $\frac{\partial F}{\partial sDIC}$ of the major EBUS. Increased winds of 0.3 m s^{-1} per 1σ NAO lead to a significant outgassing pressure of 0.05 mol m^{-2} yr^{-1}. This is due both to a large system sensitivity, $\frac{\partial F}{\partial U}$, to changes in wind and a high wind anomaly in response to the NAO. Ultimately, intensified winds and an anomalous increase in sDIC due to enhanced upwelling counteracts the solubility effects of colder SSTs. This leads to the highest relative CO_2 flux anomaly of any system, with a 21% increase in outgassing per 1σ NAO event relative to the long-term mean.

4 Summary and Conclusions

We utilize a 34-member single-model ensemble to investigate the relationship between internal climate variability and anomalous CO_2 fluxes in the major EBUS over the historical period (1920–2015). We find that the magnitude of internal variability in EBUS CO_2 fluxes is large and is only rivaled globally by the Southern Ocean and subpolar Arctic (Figure 12). For all EBUS but the CalCS, internal variability in CO_2 fluxes is larger than the seasonal cycle. The highest absolute magnitude of internal variability is in the BenCS and HumCS, with values of 0.98 mol m^{-2} yr^{-1} and 1.20 mol m^{-2} yr^{-1}, respectively (Table 11). We identify the major mode of climate variability associated with CO_2 flux residuals for three of the four systems, and then perform a linear Taylor expansion to explore how wind speed, SST, salinity, sDIC, sAlk, and freshwater fluxes individually contribute to the total anomaly. The BenCS was not analyzed in this way, due to significant model biases in alongshore winds, upwelling, and SSTs in CESM (Small et al., 2015).

We find that oscillations in the subtropical anticyclonic gyres exert the most influence on CO_2 fluxes in the CalCS and CanCS. CanCS CO_2 flux anomalies are associated mainly with the NAO, which in its positive phase reflects an intensification of the Azores High (Figure 14f). The CalCS is modulated mainly by the NPGO (Figure 14d), the oceanic expression of the atmospheric NPO, which in its positive phase describes an enhanced North Pacific High (Di Lorenzo et al., 2008). Anomalously cold waters from upwelling increase CO_2 solubility and contribute toward CO_2 uptake. The increased sDIC delivery from upwelling acts in opposition to the SST effect, contributing toward outgassing. The sDIC and SST contributions nearly exactly balance each other in the CalCS, so it is the minor contributions from winds, salinity, sAlk, and freshwater fluxes that tip the system toward a slight uptake anomaly (Figure 15). In contrast, the sDIC effect in the CanCS nearly doubles the SST effect. The outgassing pressure from increased sDIC is further reinforced by the relatively large increase in wind speed in response to the NAO and the system's high sensitivity to changes in winds, which is approximately 3 times greater than the CalCS (Figure 18). The CalCS experiences an uptake anomaly in response to enhanced upwelling-favorable gyre circulation, while the CanCS experiences increased outgassing. However, the mean state of both systems is intensified during a positive NPGO and NAO. $\frac{\partial F}{\partial U}$ is negative in the CalCS, but positive in the CanCS, i.e., increased winds drive uptake (outgassing) anomalies in the CalCS (CanCS). The sensitivity term is directly dependent on ΔpCO_2, which favors uptake (outgassing) in the CalCS (CanCS).

We also investigated the CalCS response to the PDO in two sub-regions of the system that captured its unique dipole response of anomalous uptake nearshore and outgassing offshore (Figure 16). The nearshore region experiences an uptake

anomaly which is driven by a delicate balance between reduced sDIC and warmer SSTs (Figure 16a). The offshore region experiences the same sign changes in sDIC and SST, but with contributions an order of magnitude larger in size. It is actually the reduction in sAlk offshore that contributes toward outgassing and causes the slight outgassing anomaly overall (Figure 16b). The dipole is thus not due to an inverted response of sDIC and SST to the PDO, but potentially to variability in the source waters feeding the two regions of the CalCS.

We show that CO_2 flux anomalies in the HumCS are mostly driven by ENSO (Figure 14e), due to its direct connection with the equatorial Pacific. This is largely due to our definition of the HumCS, which in fact only captures the northern HumCS. We might anticipate that the Chilean portion of the system would be more closely related to the CalCS and CanCS, and thus responsive to anticyclonic gyre oscillations due to its closer proximity to the South Pacific High. We find that the HumCS has weakened outgassing during El Niño due to a large anomalous reduction in sDIC. The sDIC response is large enough to counteract the outgassing pressure from warmer SSTs, increased winds, and reduced sAlk (Figure 17).

In summary, we find that variations in sDIC and SST exert the most influence on anomalous CO_2 fluxes in the CalCS, CanCS, and HumCS. Further, these terms always act in opposition to one another. Secondary to these terms are wind speed and sAlk. Although their contributions do not rival those of SST and sDIC in magnitude, they act to further reinforce anomalies or to tip the balance toward outgassing or uptake when sDIC and SST are of equal magnitude. In all systems, salinity and freshwater fluxes have negligible contributions toward the total CO_2 flux anomaly. The major EBUS are lumped together in many studies due to their similarities – they are all characterized by their presence on the eastern flank of subtropical gyres, their Ekman dynamics associated with this positioning which leads to coastal and curl-driven upwelling, their productive fisheries, and in the case of our study, their high variability in CO_2 fluxes. However, we show in this study that their position in terms of latitude and ocean basin as well as their coastal geometry leads to unique physical and biogeochemical responses to climate variability. In particular, despite variations in sDIC being a leading contributor to CO_2 flux anomalies, the drivers of these sDIC anomalies differ between EBUS.

Following Equation 5, Table **??** shows the absolute and Figure **??** the relative contributions of circulation (e.g., upwelling, advection, diffusion), biology (photosynthesis, respiration, and calcium carbonate formation and dissolution), and CO_2 fluxes to the approximated sDIC tendency anomalies in response to internal variability. Changes to biological activity in the HumCS in response to ENSO contribute to nearly 50% (0.861 GgC yr^{-1}) of the total sDIC tendency anomaly (Figure **??**, Table **??**). During an El Niño (La Niña) enhanced respiration (photosynthesis) pumps sDIC into (out of) the upper water column. While biology is the major contributor to sDIC tendency anomalies in the HumCS, circulation changes play a leading role in the CalCS. In response to the NPGO, circulation anomalies in the CalCS contribute to roughly 47% (0.147 GgC yr^{-1}) of the total sDIC tendency anomaly (Figure **??**, Table **??**). It is difficult to assess the relative contributions of J'_{circ} and J'_{bio} in the CanCS, as the large ensemble spread in J'_{bio} drives a highly uncertain J'_{circ}, which is computed as the residual of the other three terms (Figure **??**). In all three systems, CO_2 flux anomalies play an important role in modifying the sDIC tendency, with an ensemble mean relative contribution greater than 25% (Figure **??**).

It is important to note that anthropogenic climate change will likely modify our findings over the coming decades in a number of ways. The long-term addition of anthropogenic carbon to the surface ocean causes EBUS to become greater sinks for CO_2.

This trend shifts the mean state of the EBUS, causing historical outgassing sites (the HumCS, CanCS, and BenCS) to become intermittent net sinks of CO_2 under the influence of internal variability by the end of the historical period (Figure 13). Projecting to 2100 under RCP8.5 forcing, we find that the CanCS and BenCS become net sinks for CO_2 due to the anthropogenic trend, with mean values of -0.43 mol m^{-2} yr^{-1} and -0.04 mol m^{-2} yr^{-1} over 2016–2100, respectively. The addition of anthropogenic CO_2 into the surface ocean can also intensify the magnitude of the seasonal cycle of CO_2 flux. This is due to the increased concentration of CO_2 in the surface ocean as well as the reduction in the ocean's buffer capacity, which makes pCO_2 more sensitive to seasonal fluctuations in DIC and alkalinity (Landschützer et al., 2018, and references therein). This effect has been shown in observations (Landschützer et al., 2018) and is also projected in climate models (Kwiatkowski and Orr, 2018), but is only seen significantly in the CalCS and CanCS, with an approximate 37% and 30% increase in the CO_2 flux seasonal cycle over 2016–2100, respectively. Negligible changes to the seasonal cycle occur in the HumCS and BenCS.

External forcing will also alter the dynamics of the EBUS (Bakun et al., 2015; García-Reyes et al., 2015), potentially inducing changes to alongshore winds (Narayan et al., 2010; Sydeman et al., 2014; Oerder et al., 2015; Rykaczewski et al., 2015; Wang et al., 2015) and upper ocean stratification (Di Lorenzo et al., 2005; Rykaczewski and Dunne, 2010; Oerder et al., 2015), which will in turn influence the rate and efficacy of upwelling. However, it is unlikely that these effects will be detectable until mid-century, as the anthropogenic signal is obscured by internal variability (Brady et al., 2017). The biogeochemical signature of waters feeding upwelling (e.g., O_2, CO_2, and nutrient concentrations) will likely also be modified due to these dynamical changes as well as to changes to ocean ventilation and source water pathways (Rykaczewski and Dunne, 2010). Externally forced changes in physical and biogeochemical properties of EBUS will likely alter the relative contributions of variables to anomalous CO_2 fluxes, as approximated by Equation 4 and shown in Figures 5–8 and Table 12. It is also possible that modes of climate variability will change in response to anthropogenic forcing. Model projections and long-term observations have suggested that the intensity, frequency, or variance associated with ENSO (e.g., Timmermann et al., 1999; Cai et al., 2014, 2015), the NAO (Kuzmina et al., 2005), and the NPGO (Sydeman et al., 2013) has changed significantly in recent decades or will change over the next century. Modifications to modes of climate variability associated with the major EBUS could directly influence the magnitude of internally generated residuals in CO_2 fluxes. Further investigation of the impacts of anthropogenic climate change on CO_2 fluxes in EBUS is necessary for the community.

Our study serves as a starting point toward better understanding how internal climate variability modulates CO_2 fluxes in the major EBUS. Here, we only present the leading mode of climate variability associated with anomalous CO_2 fluxes in the HumCS and CanCS, and the leading two modes for the CalCS. Because of this, we explain approximately 16% of the total CO_2 flux variance in the HumCS and 8% in the CanCS. Since we analyzed statistically orthogonal modes (the PDO and NPGO) in the CalCS, we were able to explain as much as 31% of the total CO_2 flux variance. It is difficult to explain a large chunk of the remaining variance for the EBUS, as other modes of internal variability are physically dependent on one another. Further, locally generated atmospheric noise in the EBUS can contribute substantially to the total modeled CO_2 flux variance. Previous studies that relate anomalous CO_2 fluxes to internal climate variability have explained similar amounts of variance. For example, Lovenduski et al. (2007) explains anywhere from 2% to 31% of CO_2 flux variance in the Southern Ocean in response to the Southern Annular Mode (SAM), McKinley et al. (2006) from 6% to 38% in the North Pacific in response to the PDO, and

Gruber et al. (2002) 15% in the North Atlantic in response to the NAO. Our study is further limited by our use of a single model ensemble and by the coarseness of our climate model. The community would benefit from future studies involving multiple single-model ensembles, which would reduce uncertainty due to structural biases, such as in the dynamics of the BenCS and the elevated sub-surface DIC concentration in the east equatorial Pacific. Due to model resolution, we do not directly resolve the coastal upwelling process which induces vigorous outgassing within the first O(10km) of the coastline. This problem could be mitigated by nesting high-resolution EBUS ROMS simulations within a coarser global ensemble or by using regional mesh refinement techniques. This would allow the remote propagation of climate variability into the EBUS, while avoiding the high computational cost of running multiple high-resolution global simulations. In particular, the BenCS requires significant attention. We find pronounced internal variability in CO_2 fluxes in the BenCS in CESM-LENS that warrants investigation in a high-resolution model specific to the BenCS. We anticipate that these results and further investigation of the relationship between internal climate variability and anomalous CO_2 fluxes in EBUS will be useful for the rapidly developing subseasonal to decadal prediction community. Skillful prediction of climate variability, such as ENSO, the NPGO, and NAO, could be linked directly to anomalous fluxes of CO_2 in the major EBUS. As these systems are naturally sensitive to the undersaturation of calcium carbonate, these predictions could aid in detecting and managing the onset of seasonal ocean acidification.

Data availability. The output from CESM-LENS is available as single variable time series at monthly, daily, and 6-hourly resolution through the Earth System Grid. Instructions for access and a full listing of available variables can be found under the UCAR Large Ensemble Project web page. Also on the CESM-LENS project page is the Climate Variability Diagnostics Package (CVDP), which includes the climate indices used in this study for every simulation. Instructions for accessing the NPGO index for each simulation as well the code used to generate it can be found at http://www.cesm.ucar.edu/projects/community-projects/LENS/projects/npgo.html.

Acknowledgements. The National Science Foundation sponsors the National Center for Atmospheric Research where the Community Earth System Model is developed. Computing resources were provided by NCAR's Computational and Information Systems Laboratory. The Department of Energy's Computational Science Graduate Fellowship supported RXB throughout this study (DE-FG02-97ER25308). NSL and RXB are grateful for support from NSF (OCE-1752724, OCE-1558225). We thank A. Phillips for his extensive work on developing the Climate Variability Diagnostics Package. K. Karnauskas, J. Small, and M. Long provided feedback on earlier versions of this manuscript.

References

D. C. E. Bakker, B. Pfeil, K. M. O'Brien, K. I. Currie, S. D. Jones, C. S. Landa, S. K. Lauvset, N. Metzl, D. R. Munro, S.-I. Nakaoka, A. Olsen, D. Pierrot, S. Saito, K. Smith, C. Sweeney, T. Takahashi, C. Wada, R. Wanninkhof, S. R. Alin, M. Becker, R. G. J. Bellerby, A. V. Borges, J. Boutin, Y. Bozec, E. Burger, W.-J. Cai, R. D. Castle, C. E. Cosca, M. D. DeGrandpre, M. Donnelly, G. Eischeid, R. A. Feely, T. Gkritzalis, M. González-Dávila, C. Goyet, A. Guillot, N. J. Hardman-Mountford, J. Hauck, M. Hoppema, M. P. Humphreys, C. W. Hunt, J. S. P. Ibánhez, T. Ichikawa, M. Ishii, L. W. Juranek, V. Kitidis, A. Körtzinger, U. K. Koffi, A. Kozyr, A. Kuwata, N. Lefèvre, C. Lo Monaco, A. Manke, P. Marrec, J. T. Mathis, F. J. Millero, N. Monacci, P. M. S. Monteiro, A. Murata, T. Newberger, Y. Nojiri, I. Nonaka, A. M. Omar, T. Ono, X. A. Padín, G. Rehder, A. Rutgersson, C. L. Sabine, J. Salisbury, J. M. Santana-Casiano, D. Sasano, U. Schuster, R. Sieger, I. Skjelvan, T. Steinhoff, K. Sullivan, S. C. Sutherland, A. Sutton, K. Tadokoro, M. Telszewski, H. Thomas, B. Tilbrook, S. van Heuven, D. Vandemark, D. W. Wallace, and R. Woosley. Surface Ocean CO2 Atlas (SOCAT) V4, 2016.

A. Bakun, B. A. Black, S. J. Bograd, M. García-Reyes, A. J. Miller, R. R. Rykaczewski, and W. J. Sydeman. Anticipated effects of climate change on coastal upwelling ecosystems. *Current Climate Change Reports*, 1(2):85–93, Jun 2015. ISSN 2198-6061. https://doi.org/10.1007/s40641-015-0008-4.

R. T. Barber and F. P. Chavez. Biological consequences of El Niño. *Science*, 222(4629):1203–1210, 1983. ISSN 0036-8075. https://doi.org/10.1126/science.222.4629.1203.

R. T. Barber and F. P. Chávez. Ocean variability in relation to living resources during the 1982–83 El Niño. *Nature*, 319:279 EP –, 01 1986.

A. V. Borges and M. Frankignoulle. Distribution of surface carbon dioxide and air-sea exchange in the upwelling system off the galician coast. *Global Biogeochemical Cycles*, 16(2), 2002.

M. F. Borges, A. M. P. Santos, N. Crato, H. Mendes, and B. Mota. Sardine regime shifts off Portugal: a time series analysis of catches and wind conditions. *Scientia Marina*, 67(S1):235–244, Apr. 2003. ISSN 1886-8134, 0214-8358. https://doi.org/10.3989/scimar.2003.67s1235.

A. Boyd, J. Salat, and M. Masó. The seasonal intrusion of relatively saline water on the shelf off northern and central Namibia. *South African Journal of Marine Science*, 5(1):107–120, 1987.

R. X. Brady, M. A. Alexander, N. S. Lovenduski, and R. R. Rykaczewski. Emergent anthropogenic trends in California Current upwelling. *Geophysical Research Letters*, 44(10):5044–5052, 2017.

C. S. Bretherton, M. Widmann, V. P. Dymnikov, J. M. Wallace, and I. Bladé. The effective number of spatial degrees of freedom of a time-varying field. *Journal of Climate*, 12(7):1990–2009, 1999. https://doi.org/10.1175/1520-0442(1999)012<1990:TENOSD>2.0.CO;2.

W. Cai, S. Borlace, M. Lengaigne, P. Van Rensch, M. Collins, G. Vecchi, A. Timmermann, A. Santoso, M. J. McPhaden, L. Wu, et al. Increasing frequency of extreme el niño events due to greenhouse warming. *Nature climate change*, 4(2):111, 2014.

W. Cai, G. Wang, A. Santoso, M. J. McPhaden, L. Wu, F.-F. Jin, A. Timmermann, M. Collins, G. Vecchi, M. Lengaigne, et al. Increased frequency of extreme la niña events under greenhouse warming. *Nature Climate Change*, 5(2):132–137, 2015.

W.-J. Cai, M. Dai, and Y. Wang. Air-sea exchange of carbon dioxide in ocean margins: A province-based synthesis. *Geophysical Research Letters*, 33(12), 2006. https://doi.org/10.1029/2006GL026219.

F. Chan, J. A. Barth, C. A. Blanchette, R. H. Byrne, F. Chavez, O. Cheriton, R. A. Feely, G. Friederich, B. Gaylord, T. Gouhier, S. Hacker, T. Hill, G. Hofmann, M. A. McManus, B. A. Menge, K. J. Nielsen, A. Russell, E. Sanford, J. Sevadjian, and L. Washburn. Persistent spatial structuring of coastal ocean acidification in the california current system. *Scientific Reports*, 7(1):2526, 2017. https://doi.org/10.1038/s41598-017-02777-y.

F. P. Chavez and M. Messié. A comparison of eastern boundary upwelling ecosystems. *Progress in Oceanography*, 83(1):80–96, 2009. https://doi.org/https://doi.org/10.1016/j.pocean.2009.07.032.

F. P. Chavez, J. T. Pennington, C. G. Castro, J. P. Ryan, R. P. Michisaki, B. Schlining, P. Walz, K. R. Buck, A. McFadyen, and C. A. Collins. Biological and chemical consequences of the 1997–1998 el niño in central california waters. *Progress in Oceanography*, 54(1):205–232, 2002. https://doi.org/https://doi.org/10.1016/S0079-6611(02)00050-2.

D. B. Chelton, P. A. Bernal, and J. A. McGowan. Large-scale interannual physical and biological interaction in the california current. *Journal of Marine Research*, 40(4):1095–1125, 1982.

F. Chenillat, P. Rivière, X. Capet, E. Di Lorenzo, and B. Blanke. North pacific gyre oscillation modulates seasonal timing and ecosystem functioning in the california current upwelling system. *Geophysical Research Letters*, 39(1), 2012. https://doi.org/10.1029/2011GL049966.

K. Chhak and E. Di Lorenzo. Decadal variations in the california current upwelling cells. *Geophysical Research Letters*, 34(14), 2007. https://doi.org/10.1029/2007GL030203.

F. Colas, X. Capet, J. McWilliams, and A. Shchepetkin. 1997–1998 el niño off peru: A numerical study. *Progress in Oceanography*, 79(2-4): 138–155, 2008.

T. E. Cropper, E. Hanna, and G. R. Bigg. Spatial and temporal seasonal trends in coastal upwelling off northwest africa, 1981–2012. *Deep Sea Research Part I: Oceanographic Research Papers*, 86:94–111, 2014. https://doi.org/https://doi.org/10.1016/j.dsr.2014.01.007.

M. D. DeGrandpre, T. R. Hammar, and C. D. Wirick. Short-term pco2 and o2 dynamics in california coastal waters. *Deep Sea Research Part II: Topical Studies in Oceanography*, 45(8):1557–1575, 1998. https://doi.org/https://doi.org/10.1016/S0967-0645(98)80006-4.

C. Deser, I. R. Simpson, K. A. McKinnon, and A. S. Phillips. The northern hemisphere extratropical atmospheric circulation response to enso: How well do we know it and how do we evaluate models accordingly? *Journal of Climate*, 30(13):5059–5082, 2017.

C. Deser, I. R. Simpson, A. S. Phillips, and K. A. McKinnon. How well do we know enso's climate impacts over north america, and how do we evaluate models accordingly? *Journal of Climate*, 2018.

E. Di Lorenzo and N. Mantua. Multi-year persistence of the 2014/15 north pacific marine heatwave. *Nature Climate Change*, 6(11): 1042–1047, 2016.

E. Di Lorenzo, A. J. Miller, N. Schneider, and J. C. McWilliams. The warming of the california current system: Dynamics and ecosystem implications. *Journal of Physical Oceanography*, 35(3):336–362, 2005.

E. Di Lorenzo, N. Schneider, K. M. Cobb, P. J. S. Franks, K. Chhak, A. J. Miller, J. C. McWilliams, S. J. Bograd, H. Arango, E. Curchitser, T. M. Powell, and P. Rivière. North pacific gyre oscillation links ocean climate and ecosystem change. *Geophysical Research Letters*, 35 (8), 2008. https://doi.org/10.1029/2007GL032838.

E. Di Lorenzo, J. Fiechter, N. Schneider, A. Bracco, A. J. Miller, P. J. S. Franks, S. J. Bograd, A. M. Moore, A. C. Thomas, W. Crawford, A. Peña, and A. J. Hermann. Nutrient and salinity decadal variations in the central and eastern north pacific. *Geophysical Research Letters*, 36(14), 2009. https://doi.org/10.1029/2009GL038261.

D. Enfield. Thermally driven wind variability in the planetary boundary layer above lima, peru. *Journal of Geophysical Research: Oceans*, 86(C3):2005–2016, 1981.

R. Escribano, G. Daneri, L. Farías, V. A. Gallardo, H. E. González, D. Gutiérrez, C. B. Lange, C. E. Morales, O. Pizarro, O. Ulloa, and M. Braun. Biological and chemical consequences of the 1997–1998 el niño in the chilean coastal upwelling system: a synthesis. *Deep Sea Research Part II: Topical Studies in Oceanography*, 51(20):2389–2411, 2004. https://doi.org/https://doi.org/10.1016/j.dsr2.2004.08.011.

W. Evans, B. Hales, and P. G. Strutton. Seasonal cycle of surface ocean pco2 on the oregon shelf. *Journal of Geophysical Research: Oceans*, 116(C5), 2011. https://doi.org/10.1029/2010JC006625.

G. E. Friederich, P. M. Walz, M. G. Burczynski, and F. P. Chavez. Inorganic carbon in the central california upwelling system during the 1997–1999 el niño–la niña event. *Progress in Oceanography*, 54(1):185–203, 2002. https://doi.org/https://doi.org/10.1016/S0079-6611(02)00049-6.

M. Frischknecht, M. Münnich, and N. Gruber. Remote versus local influence of enso on the california current system. *Journal of Geophysical Research: Oceans*, 120(2):1353–1374, 2015. https://doi.org/10.1002/2014JC010531.

M. Frischknecht, M. Münnich, and N. Gruber. Local atmospheric forcing driving an unexpected california current system response during the 2015–2016 el niño. *Geophysical Research Letters*, 44(1):304–311, 2017. https://doi.org/10.1002/2016GL071316.

M. García-Reyes, W. J. Sydeman, D. S. Schoeman, R. R. Rykaczewski, B. A. Black, A. J. Smit, and S. J. Bograd. Under pressure: Climate change, upwelling, and eastern boundary upwelling ecosystems. *Frontiers in Marine Science*, 2:109, 2015.

P. R. Gent, S. G. Yeager, R. B. Neale, S. Levis, and D. A. Bailey. Improvements in a half degree atmosphere/land version of the ccsm. *Climate Dynamics*, 34(6):819–833, 2010.

M. González-Dávila, J. M. Santana-Casiano, and I. R. Ucha. Seasonal variability of fco2 in the angola-benguela region. *Progress in Oceanography*, 83(1-4):124–133, 2009.

L. Gregor and P. Monteiro. Is the southern benguela a significant regional sink of co2? *South African Journal of Science*, 109(5-6):01–05, 2013.

N. Gruber. Carbon at the coastal interface. *Nature; London*, 517(7533):148–149, Jan. 2015. ISSN 00280836.

N. Gruber, C. D. Keeling, and N. R. Bates. Interannual variability in the north atlantic ocean carbon sink. *Science*, 298(5602):2374–2378, 2002. ISSN 0036-8075. https://doi.org/10.1126/science.1077077.

B. Hales, T. Takahashi, and L. Bandstra. Atmospheric co2 uptake by a coastal upwelling system. *Global Biogeochemical Cycles*, 19(1), 2005. https://doi.org/10.1029/2004GB002295.

J. Hauck. Unsteady seasons in the sea. *Nature Climate Change*, 8(2):97–98, 2018. https://doi.org/10.1038/s41558-018-0069-1.

C. Hauri, N. Gruber, G.-K. Plattner, S. Alin, R. A. Feely, B. Hales, and P. A. Wheeler. Ocean Acidification in the California Current System. *Oceanography*, 22(4):60–71, Dec. 2009.

A. Huyer, R. L. Smith, and T. Paluszkiewicz. Coastal upwelling off peru during normal and el niño times, 1981–1984. *Journal of Geophysical Research: Oceans*, 92(C13):14297–14307, 1987.

M. G. Jacox, S. J. Bograd, E. L. Hazen, and J. Fiechter. Sensitivity of the california current nutrient supply to wind, heat, and remote ocean forcing. *Geophysical Research Letters*, 42(14):5950–5957, 2015.

J. E. Kay, C. Deser, A. Phillips, A. Mai, C. Hannay, G. Strand, J. M. Arblaster, S. C. Bates, G. Danabasoglu, J. Edwards, M. Holland, P. Kushner, J.-F. Lamarque, D. Lawrence, K. Lindsay, A. Middleton, E. Munoz, R. Neale, K. Oleson, L. Polvani, and M. Vertenstein. The community earth system model (cesm) large ensemble project: A community resource for studying climate change in the presence of internal climate variability. *Bulletin of the American Meteorological Society*, 96(8):1333–1349, 2015. https://doi.org/10.1175/BAMS-D-13-00255.1.

A. W. King, L. Dilling, G. P. Zimmerman, D. M. Fairman, R. A. Houghton, G. Marland, A. Z. Rose, and T. J. Wilbanks. *The first state of the carbon cycle report (SOCCR): The North American carbon budget and implications for the global carbon cycle. ID - 20083154843*. U.S. Climate Change Science Program, Washington, 2007.

S. I. Kuzmina, L. Bengtsson, O. M. Johannessen, H. Drange, L. P. Bobylev, and M. W. Miles. The north atlantic oscillation and greenhouse-gas forcing. *Geophysical Research Letters*, 32(4), 2005.

L. Kwiatkowski and J. C. Orr. Diverging seasonal extremes for ocean acidification during the twenty-first century. *Nature Climate Change*, 8(2):141–145, 2018. https://doi.org/10.1038/s41558-017-0054-0.

P. Landschützer, N. Gruber, D. C. E. Bakker, U. Schuster, S. Nakaoka, M. R. Payne, T. P. Sasse, and J. Zeng. A neural network-based estimate of the seasonal to inter-annual variability of the Atlantic Ocean carbon sink. *Biogeosciences*, 10(11):7793–7815, Nov. 2013. ISSN 1726-4189. https://doi.org/10.5194/bg-10-7793-2013.

P. Landschützer, N. Gruber, and D. C. E. Bakker. Decadal variations and trends of the global ocean carbon sink. *Global Biogeochemical Cycles*, 30(10):1396–1417, 2016. ISSN 1944-9224. https://doi.org/10.1002/2015GB005359.

P. Landschützer, N. Gruber, and D. C. E. Bakker. An updated observation-based global monthly gridded sea surface pco2 and air-sea co2 flux product from 1982 through 2015 and its monthly climatology (ncei accession 0160558). Version 2.2. NOAA National Centers for Environmental Information. Dataset., July 2017.

P. Landschützer, N. Gruber, D. C. E. Bakker, I. Stemmler, and K. D. Six. Strengthening seasonal marine CO2 variations due to increasing atmospheric CO2. *Nature Climate Change*, Jan. 2018. ISSN 1758-678X, 1758-6798. https://doi.org/10.1038/s41558-017-0057-x.

G. G. Laruelle, H. H. Dürr, C. P. Slomp, and A. V. Borges. Evaluation of sinks and sources of CO2 in the global coastal ocean using a spatially-explicit typology of estuaries and continental shelves. *Geophysical Research Letters*, 37(15), Aug. 2010. ISSN 00948276. https://doi.org/10.1029/2010GL043691.

G. G. Laruelle, R. Lauerwald, B. Pfeil, and P. Regnier. Regionalized global budget of the CO2 exchange at the air-water interface in continental shelf seas. *Global Biogeochem. Cycles*, 28(11):2014GB004832, Nov. 2014. ISSN 1944-9224. https://doi.org/10.1002/2014GB004832.

G. G. Laruelle, P. Landschützer, N. Gruber, J.-L. Tison, B. Delille, and P. Regnier. Global high-resolution monthly p co 2 climatology for the coastal ocean derived from neural network interpolation. *Biogeosciences*, 14(19):4545, 2017.

A. Leinweber, N. Gruber, H. Frenzel, G. E. Friederich, and F. P. Chavez. Diurnal carbon cycling in the surface ocean and lower atmosphere of Santa Monica Bay, California. *Geophysical Research Letters*, 36(8), Apr. 2009. ISSN 0094-8276. https://doi.org/10.1029/2008GL037018.

N. Lovenduski, M. Long, and K. Lindsay. Natural variability in the surface ocean carbonate ion concentration. *Biogeosciences*, 12(21): 6321–6335, 2015.

N. S. Lovenduski and N. Gruber. Impact of the Southern Annular Mode on Southern Ocean circulation and biology. *Geophys. Res. Lett.*, 32 (11):L11603, June 2005. ISSN 1944-8007. https://doi.org/10.1029/2005GL022727.

N. S. Lovenduski, N. Gruber, S. C. Doney, and I. D. Lima. Enhanced CO2 outgassing in the Southern Ocean from a positive phase of the Southern Annular Mode. *Global Biogeochem. Cycles*, 21(2), June 2007. ISSN 1944-9224. https://doi.org/10.1029/2006GB002900.

N. S. Lovenduski, G. A. McKinley, A. R. Fay, K. Lindsay, and M. C. Long. Partitioning uncertainty in ocean carbon uptake projections: Internal variability, emission scenario, and model structure. *Global Biogeochemical Cycles*, 30(9):1276–1287, 2016.

R. Lynn and S. Bograd. Dynamic evolution of the 1997–1999 El Niño–La Niña cycle in the southern California Current System. *Progress in Oceanography*, 54(1-4):59–75, July 2002. ISSN 00796611. https://doi.org/10.1016/S0079-6611(02)00043-5.

N. J. Mantua and S. R. Hare. The pacific decadal oscillation. *Journal of oceanography*, 58(1):35–44, 2002.

N. J. Mantua, S. R. Hare, Y. Zhang, J. M. Wallace, and R. C. Francis. A Pacific Interdecadal Climate Oscillation with Impacts on Salmon Production. *Bulletin of the American Meteorological Society*, 78(6):1069–1079, June 1997. ISSN 0003-0007. https://doi.org/10.1175/1520-0477(1997)078<1069:APICOW>2.0.CO;2.

G. A. McKinley, T. Takahashi, E. Buitenhuis, F. Chai, J. R. Christian, S. C. Doney, M.-S. Jiang, K. Lindsay, J. K. Moore, C. Le Quere, et al. North pacific carbon cycle response to climate variability on seasonal to decadal timescales. *Journal of Geophysical Research: Oceans*, 111(C7), 2006.

R. Mogollón and P. H. Calil. On the effects of enso on ocean biogeochemistry in the northern humboldt current system (nhcs): A modeling study. *Journal of Marine Systems*, 172:137–159, 2017.

I. Montes, W. Schneider, F. Colas, B. Blanke, and V. Echevin. Subsurface connections in the eastern tropical pacific during la niña 1999–2001 and el niño 2002–2003. *Journal of Geophysical Research: Oceans*, 116(C12), 2011.

N. Narayan, A. Paul, S. Mulitza, and M. Schulz. Trends in coastal upwelling intensity during the late 20th century. *Ocean Science*, 6(3):815, 2010.

V. Oerder, F. Colas, V. Echevin, F. Codron, J. Tam, and A. Belmadani. Peru-chile upwelling dynamics under climate change. *Journal of Geophysical Research: Oceans*, 120(2):1152–1172, 2015.

M. Pozo Buil and E. Di Lorenzo. Decadal dynamics and predictability of oxygen and subsurface tracers in the california current system. *Geophysical Research Letters*, 44(9):4204–4213, 2017.

C. Reason, P. Florenchie, M. Rouault, and J. Veitch. Influences of large scale climate modes and agulhas system variability on the BCLME region. In *Large Marine Ecosystems*, volume 14, pages 223–238. Elsevier, 2006. ISBN 978-0-444-52759-2. https://doi.org/10.1016/S1570-0461(06)80015-7.

R. R. Rykaczewski and J. P. Dunne. Enhanced nutrient supply to the california current ecosystem with global warming and increased stratification in an earth system model. *Geophysical Research Letters*, 37(21), 2010.

R. R. Rykaczewski, J. P. Dunne, W. J. Sydeman, M. García-Reyes, B. A. Black, and S. J. Bograd. Poleward displacement of coastal upwelling-favorable winds in the ocean's eastern boundary currents through the 21st century. *Geophysical Research Letters*, 42(15): 6424–6431, 2015.

J. H. Ryther. Photosynthesis and fish production in the sea. *Science*, 166(3901):72–76, 1969.

J. M. Santana-Casiano, M. González-Dávila, M.-J. Rueda, O. Llinás, and E.-F. González-Dávila. The interannual variability of oceanic co2 parameters in the northeast atlantic subtropical gyre at the estoc site. *Global Biogeochemical Cycles*, 21(1), 2007.

R. J. Small, E. Curchitser, K. Hedstrom, B. Kauffman, and W. G. Large. The benguela upwelling system: Quantifying the sensitivity to resolution and coastal wind representation in a global climate model. *Journal of Climate*, 28(23):9409–9432, 2015.

P. T. Strub, J. Mesias, V. Montecino, J. Rutllant, and S. Marchant. Coastal Ocean Circulation Off Western South America. In *The Sea*, volume 11. John Wiley, New York, 1998.

W. Sydeman, M. García-Reyes, D. Schoeman, R. Rykaczewski, S. Thompson, B. Black, and S. Bograd. Climate change and wind intensification in coastal upwelling ecosystems. *Science*, 345(6192):77–80, 2014.

W. J. Sydeman, J. A. Santora, S. A. Thompson, B. Marinovic, and E. D. Lorenzo. Increasing variance in north pacific climate relates to unprecedented ecosystem variability off california. *Global Change Biology*, 19(6):1662–1675, 2013.

T. Takahashi, S. C. Sutherland, R. Wanninkhof, C. Sweeney, R. A. Feely, D. W. Chipman, B. Hales, G. Friederich, F. Chavez, C. Sabine, A. Watson, D. C. E. Bakker, U. Schuster, N. Metzl, H. Yoshikawa-Inoue, M. Ishii, T. Midorikawa, Y. Nojiri, A. Körtzinger, T. Steinhoff, M. Hoppema, J. Olafsson, T. S. Arnarson, B. Tilbrook, T. Johannessen, A. Olsen, R. Bellerby, C. S. Wong, B. Delille, N. R. Bates, and H. J. W. de Baar. Climatological mean and decadal change in surface ocean pCO2, and net sea–air CO2 flux over the global oceans. *Deep Sea Research Part II: Topical Studies in Oceanography*, 56(8):554–577, Apr. 2009. ISSN 0967-0645. https://doi.org/10.1016/j.dsr2.2008.12.009.

D. W. J. Thompson, E. A. Barnes, C. Deser, W. E. Foust, and A. S. Phillips. Quantifying the role of internal climate variability in future climate trends. *Journal of Climate*, 28(16):6443–6456, 2015. https://doi.org/10.1175/JCLI-D-14-00830.1.

A. Timmermann, J. Oberhuber, A. Bacher, M. Esch, M. Latif, and E. Roeckner. Increased el niño frequency in a climate model forced by future greenhouse warming. *Nature*, 398(6729):694, 1999.

G. Turi, Z. Lachkar, and N. Gruber. Spatiotemporal variability and drivers of pCO2 and air–sea CO2 fluxes in the California Current System: an eddy-resolving modeling study. *Biogeosciences*, 11(3):671–690, Feb. 2014. ISSN 1726-4189. https://doi.org/10.5194/bg-11-671-2014.

G. Turi, M. A. Alexander, N. S. Lovenduski, A. Capotondi, J. D. Scott, C. A. Stock, J. P. Dunne, J. John, and M. G. Jacox. Response of O2 and pH to ENSO in the California Current System in a high resolution global climate model. *Ocean Sciences Discussion*, Aug. 2017.

D. Wang, T. C. Gouhier, B. A. Menge, and A. R. Ganguly. Intensification and spatial homogenization of coastal upwelling under climate change. *Nature*, 518(7539):390, 2015.

R. Wanninkhof. Relationship between wind speed and gas exchange over the ocean revisited: Gas exchange and wind speed over the ocean. *Limnology and Oceanography: Methods*, 12(6):351–362, June 2014. ISSN 15415856. https://doi.org/10.4319/lom.2014.12.351.

K. Wyrtki. El niño—the dynamic response of the equatorial pacific oceanto atmospheric forcing. *Journal of Physical Oceanography*, 5(4): 572–584, 1975.

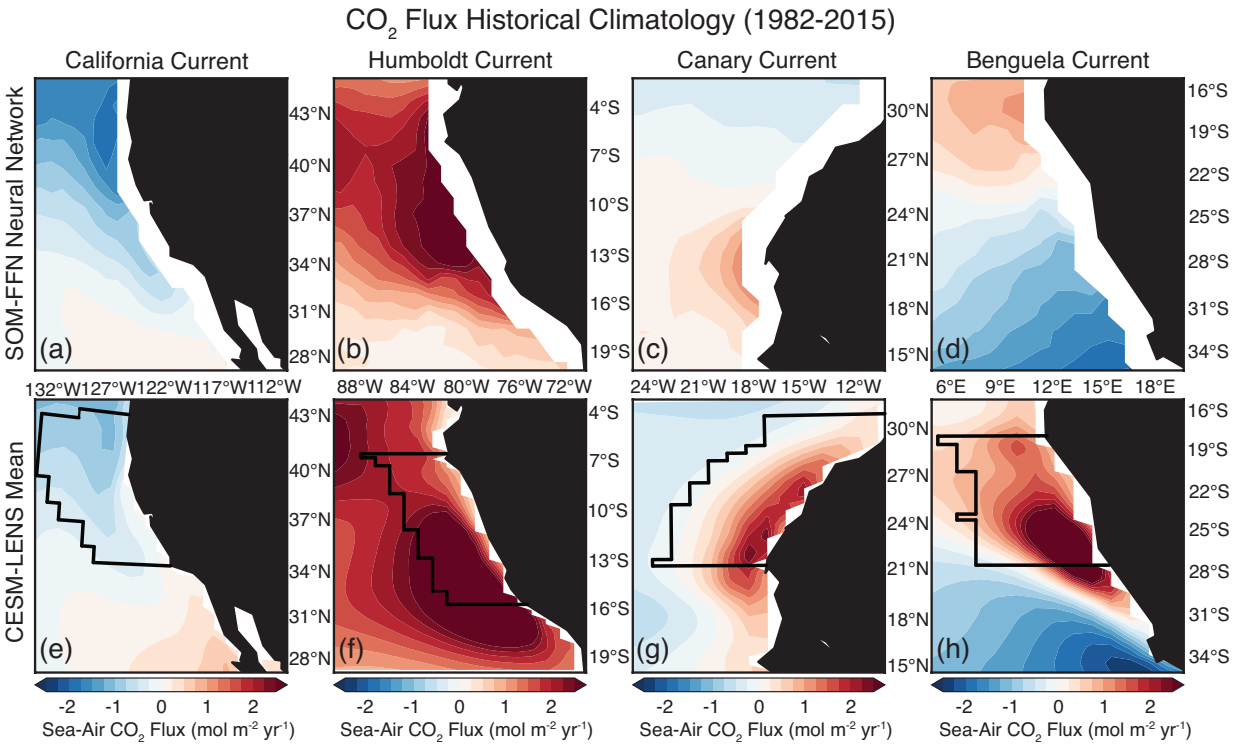

Figure 11. Comparison of CO_2 flux climatology from 1982–2015 between the SOM-FFN (a–d) and the CESM-LENS (e–h). Red denotes outgassing of CO_2 from the ocean to the atmosphere, while blue represents uptake of CO_2 by the ocean. Black lines in e–h follow the model grid and show the region used in each EBUS for statistical analysis, which is based on the 10^o latitude of most active upwelling from Chavez and Messié (2009) and confined to 800km offshore.

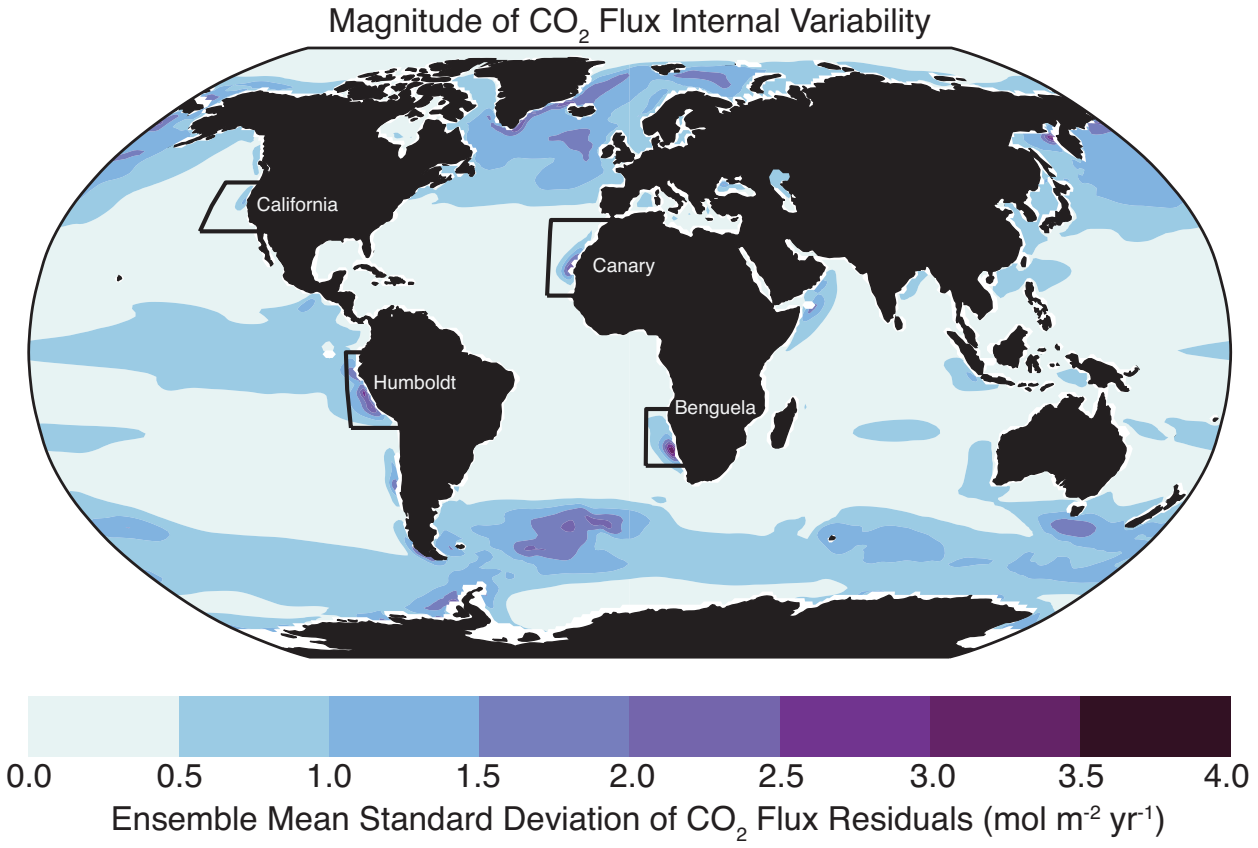

Figure 12. Magnitude of internal variability in CO_2 flux from 1920–2015 in the CESM-LENS. Residuals were generated by removing the ensemble mean – which represents the seasonality and forced signal – from each realization. Internal variability was then quantified by taking the ensemble mean standard deviation of the residuals from 1920–2015.

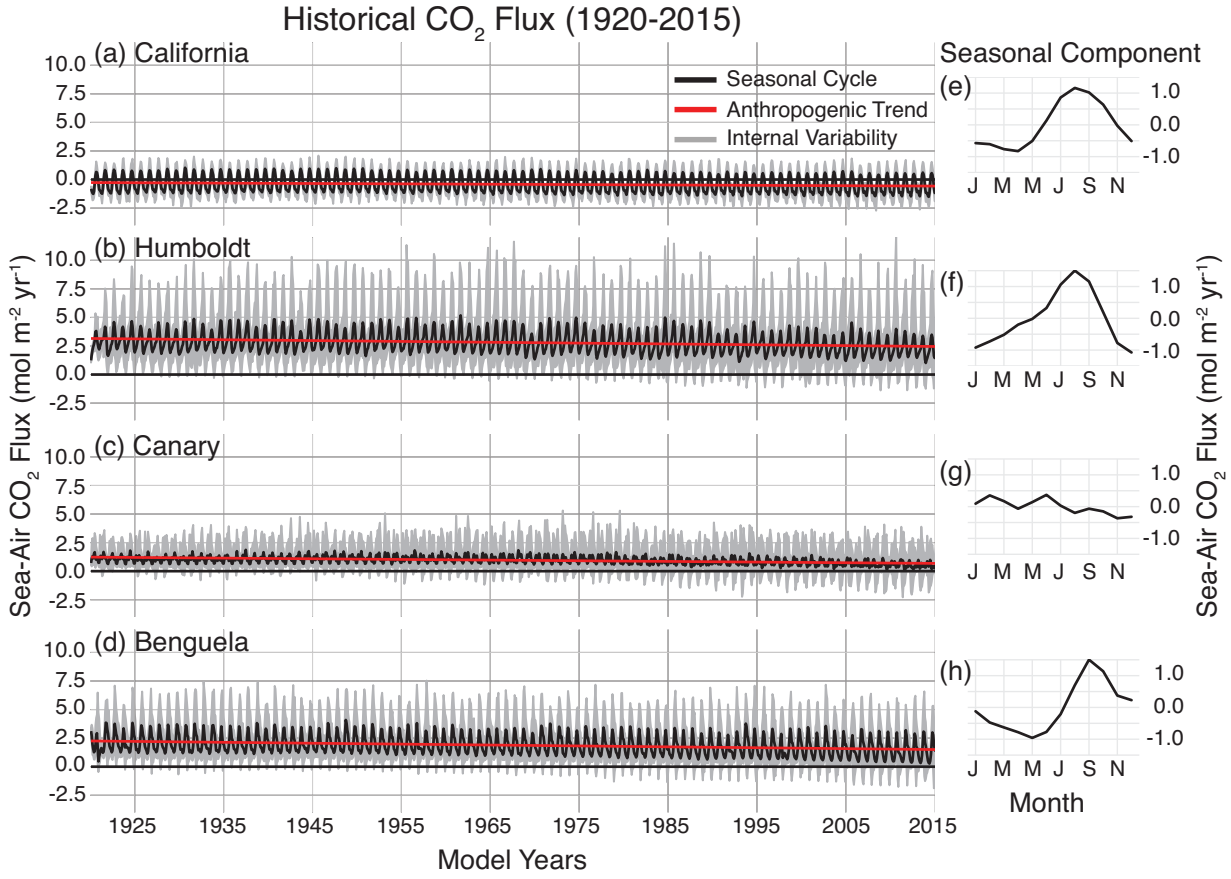

Figure 13. Time series of historical CO_2 flux (1920–2015) in the CESM-LENS for each of the four studied upwelling systems (a–d). The ensemble mean yields both the seasonal cycle (black) and the anthropogenic trend (red). Gray shading shows the bounds of the maximum and minimum realizations due to internal variability. Table 11 displays the intercept, seasonality, internal variability, and anthropogenic trend for each system. Plots e–h show the mean seasonal cycle for 1920–2015 for each system.

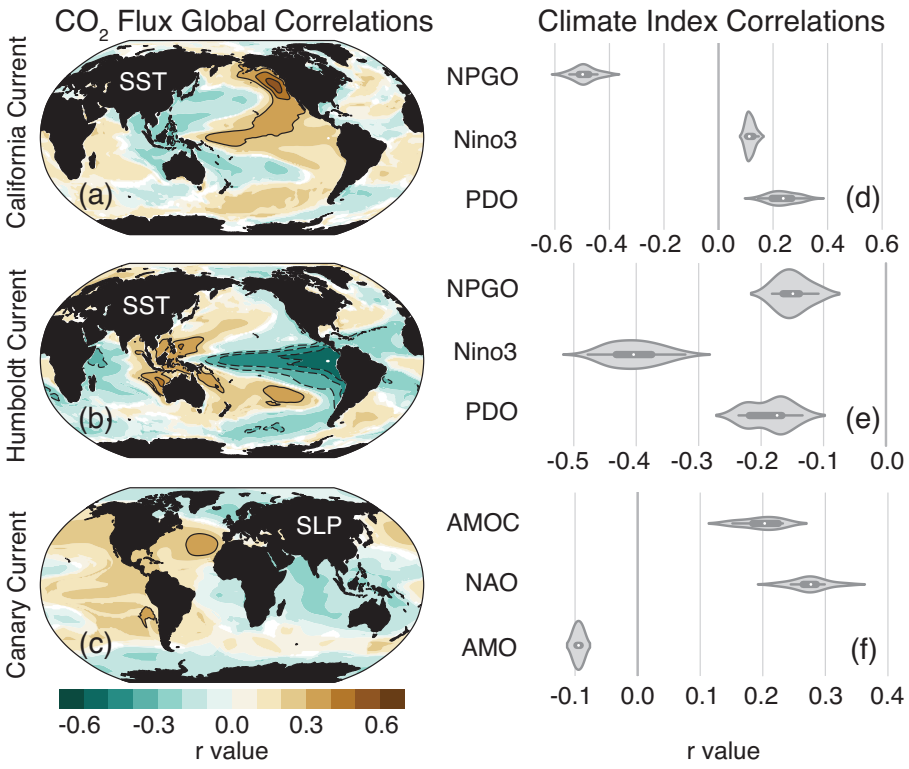

Figure 14. Correlations between area–weighted CO_2 flux residuals in the statistical study regions outlined in black in Figure 11 (e–g) and SSTa (a–b; California, Humboldt) and SLPa (c; Canary) grid cells globally. Brown colors indicate that positive values of SSTa/SLPa correlate with outgassing, and blue with uptake. Contour lines begin at $\pm$ 0.3 and progress in intervals of 0.1. Correlations were performed for each realization individually and the ensemble mean of those global correlations are presented here.

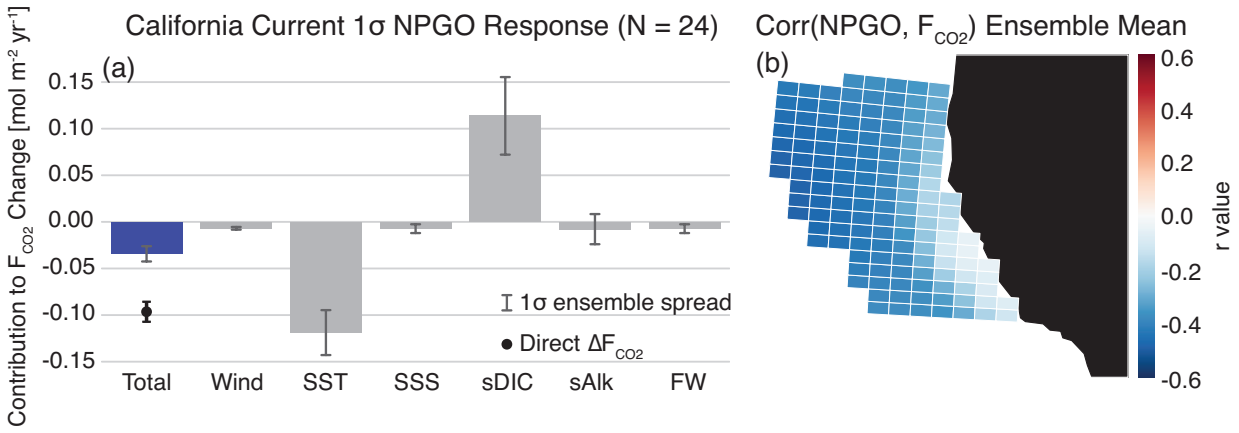

Figure 15. Linear Taylor expansion from Eq. (4) for CalCS CO_2 flux residuals regressed onto the NPGO (a). Gray bars represent the ensemble mean contributions of each variable to the CO_2 flux anomaly. Error bars represent the one standard deviation spread of the full ensemble. The individual bars sum to the "total" bar to approximate the direct regression of ΔF_{CO_2} onto the NPGO, which is denoted as the black dot with its associated ensemble spread. The ensemble mean grid cell correlations between CO_2 flux residuals and the NPGO in the CalCS study region are displayed in (b). Positive correlations are associated with outgassing, negative with uptake. Values and ensemble spread for each bar are presented in Table 12.

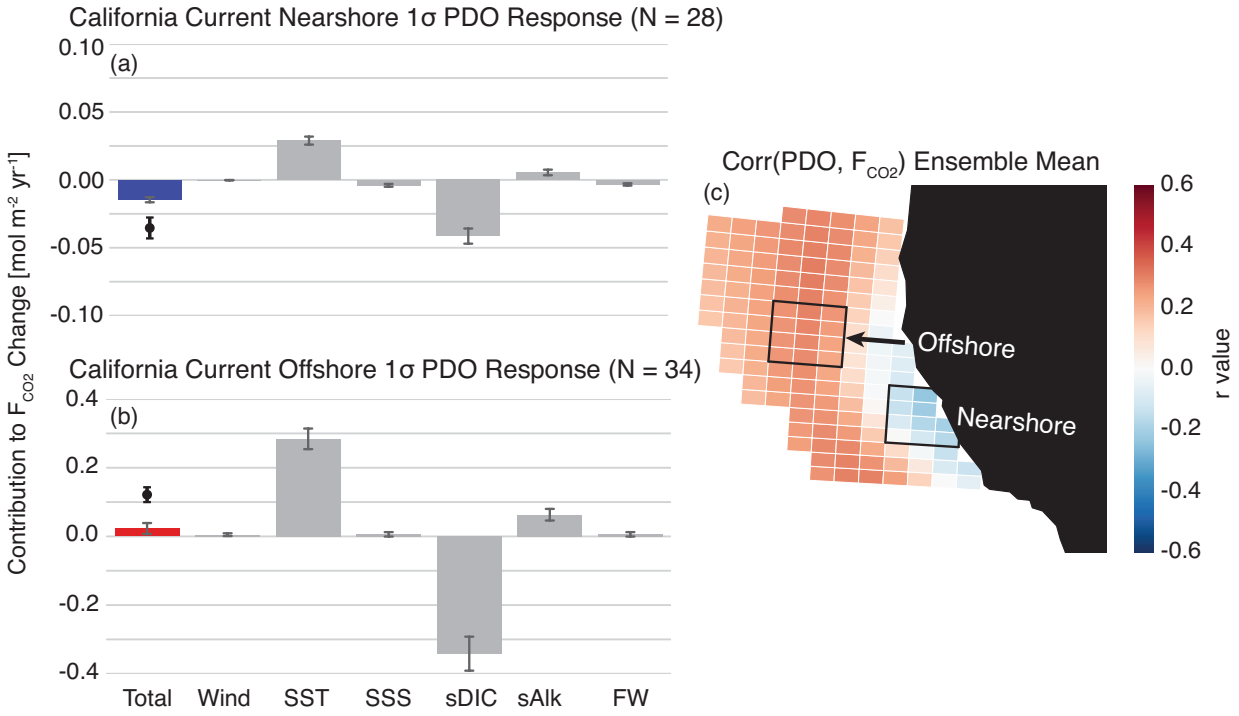

Figure 16. As in Figure 15, but in response to the PDO for a nearshore region (a) and offshore region (b). Note that the offshore decomposition (b) has a y-axis range four times that of the nearshore decomposition (a).

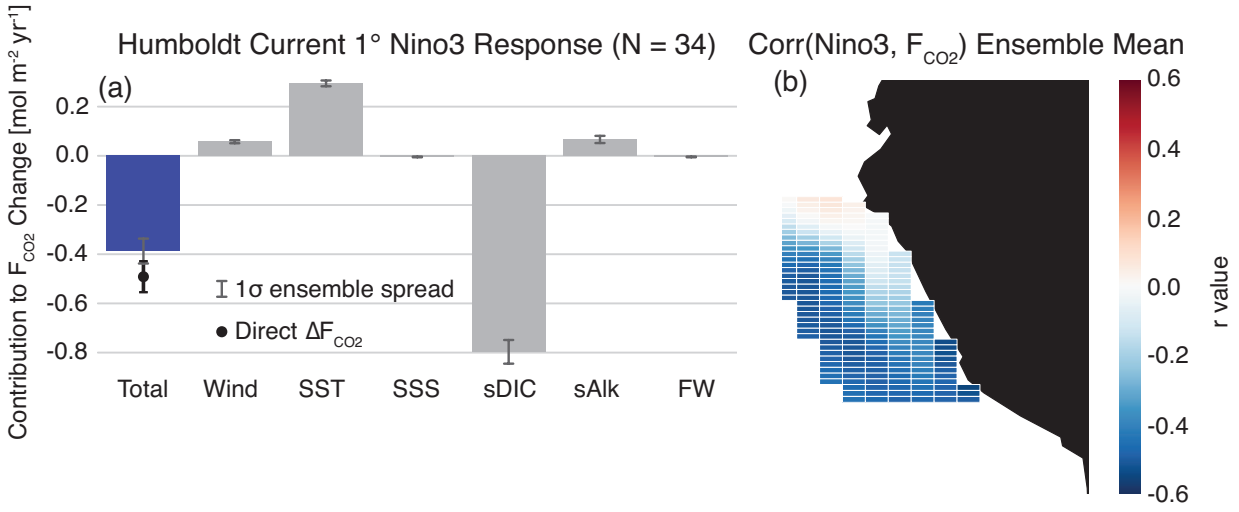

Figure 17. As in Figure 15, but for the Humboldt Current response to the Nino3 index.

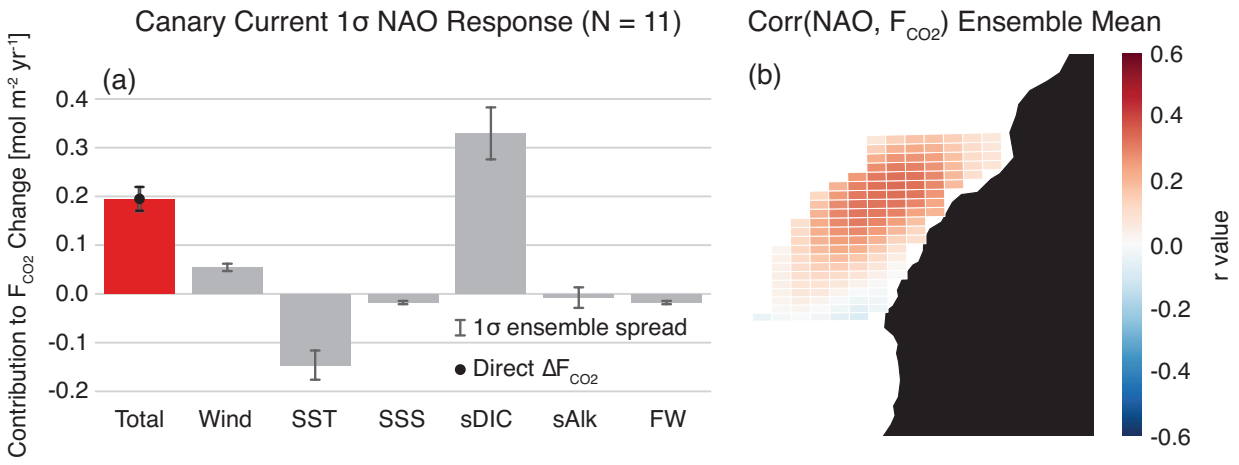

Figure 18. As in Figure 15, but for the Canary Current response to the NAO.

Table 11. Statistics for CO_2 fluxes in the CalCS, HumCS, CanCS, and BenCS from 1920–2015. The seasonal component is computed as the standard deviation of the ensemble mean after removing a fourth-order polynomial fit to remove the anthropogenic trend. The internal component is computed as the ensemble mean standard deviation of the residuals. The trend is computed as the first-order ordinary least squares regression coefficient. The intercept is derived from this linear regression.

Upwelling System	Intercept[1]	Seasonal[1]	Internal[1]	Trend[23]	Non-Seasonal Component (%)
California (34^o N–44^o N)	-0.27	0.71	0.33	-0.31	31
Humboldt (16^o S–6^o S)	3.16	0.83	1.20	-0.71	59
Canary (21^o N–31^o N)	1.23	0.23	0.62	-0.56	73
Benguela (28^o S–18^o S)	2.25	0.77	0.98	-0.76	56

[1] mol m^{-2} yr^{-1}

[2] mol m^{-2} yr^{-1} 96yr^{-1}

[3] All trends are significant to α = 0.05 for a one-sided Mann-Kendall Test

Table 12. Estimated contributions to CO_2 flux anomalies, ΔF using Eq. (4).

Quantity	CalCS – NPGO	CalCS – PDOo	CalCS – PDOn	HumCS – Nino3	CanCS – NAO
			Individual Terms		
$\frac{\partial F}{\partial U}\Delta U$	-0.01 $\pm$ 0.0	0.01 $\pm$ 0.0	0.0 $\pm$ 0.0	0.06 $\pm$ 0.01	0.05 $\pm$ 0.01
$\frac{\partial F}{\partial T}\Delta T$	-0.12 $\pm$ 0.02	0.28 $\pm$ 0.03	0.03 $\pm$ 0.0	0.29 $\pm$ 0.01	-0.15 $\pm$ 0.03
$\frac{\partial F}{\partial S}\Delta S$	-0.01 $\pm$ 0.0	0.01 $\pm$ 0.01	0.0 $\pm$ 0.0	-0.0 $\pm$ 0.0	-0.02 $\pm$ 0.0
$\frac{S}{S_0}\frac{\partial F}{\partial DIC}\Delta sDIC$	0.11 $\pm$ 0.04	-0.34 $\pm$ 0.05	-0.04 $\pm$ 0.01	-0.8 $\pm$ 0.05	0.33 $\pm$ 0.05
$\frac{S}{S_0}\frac{\partial F}{\partial Alk}\Delta sAlk$	-0.01 $\pm$ 0.02	0.06 $\pm$ 0.02	0.01 $\pm$ 0.0	0.07 $\pm$ 0.01	-0.01 $\pm$ 0.02
$\frac{\partial F}{\partial fw}\Delta fw$	-0.01 $\pm$ 0.0	0.01 $\pm$ 0.01	0.0 $\pm$ 0.0	0.0 $\pm$ 0.0	-0.02 $\pm$ 0.0
			Sum of Terms Versus Modeled		
Σ	-0.03 $\pm$ 0.01	0.02 $\pm$ 0.02	-0.01 $\pm$ 0.0	-0.38 $\pm$ 0.05	0.21 $\pm$ 0.03
ΔF_{mod}	-0.10 $\pm$ 0.01	0.12 $\pm$ 0.02	-0.04 $\pm$ 0.01	-0.49 $\pm$ 0.06	0.2 $\pm$ 0.02